Journal of Catalysis 276 (2010) 56–65

Contents lists available at ScienceDirect

Journal of Catalysis

journal homepage: www.elsevier.com/locate/jcat

Cr–MnO_x mixed-oxide catalysts for selective catalytic reduction of NO_x with NH_3 at low temperature

Zhihang Chen [a], Qing Yang [a], Hua Li [a], Xuehui Li [a,*], Lefu Wang [a], Shik Chi Tsang [b,**]

[a] School of Chemistry and Chemical Engineering, The Guangdong Province Laboratory of Green Chemical Technology, South China University of Technology, Guangzhou 510640, PR China
[b] Wolfson Catalysis Centre, Inorganic Chemistry Laboratory, University of Oxford, Oxford OX1 3QR, UK

ARTICLE INFO

Article history:
Received 1 May 2010
Revised 30 July 2010
Accepted 28 August 2010

Keywords:
Cr–Mn mixed oxide
Low temperature
Selective catalytic reduction
Nitrogen oxides
$CrMn_{1.5}O_4$

ABSTRACT

Cr–Mn mixed-oxide based catalysts were prepared for the low-temperature selective catalytic reduction of NO_x with ammonia in the presence of excess oxygen. It was found that the Cr(0.4)–MnO_x showed the highest activity and yielded 98.5% NO_x conversion at 120 °C. XRD, TPR and Raman data results suggested that a crystalline phase of $CrMn_{1.5}O_4$ was present in the Cr–MnO_x catalysts, which contained the active species. XPS results of fresh, used and regenerated Cr(0.4)–MnO_x catalysts illustrated clearly the presence of Mn^{2+}, Mn^{3+}, Mn^{4+} and Cr^{2+}, Cr^{3+}, Cr^{5+} oxidation states. Efficient electron transfer between Cr and Mn in the crystal of $CrMn_{1.5}O_4$ was thought to be the reason for the high activity and long lifetime of the Cr(0.4)–MnO_x catalyst. In addition, the SCR activity was gradually suppressed in the presence of SO_2, while such an effect was shown to be reversible after switching off the SO_2 injection.

1. Introduction

Nitrogen oxides (NO, NO_2 and N_2O) resulting from fossil fuel combustion have been a major source of air pollution. These oxides have caused environmental problems such as photochemical smog, acid rain, ozone depletion and greenhouse effects. At present, about 49% of NO_x from transportation and 46% from power plants are recorded [1]. Several methods have been used for the elimination of NO_x, such as selective catalytic reduction (SCR) [2–4], catalytic decomposition [5,6] and plasma catalysis [7,8]. SCR of NO_x with NH_3 is an effective technique and has been commercialized in the post-treatment of flue gases of power plants. In this process, NO_x from flue gases is reduced by ammonia in excess oxygen to molecular nitrogen and water:

$$4NO + 4NH_3 + O_2 \rightarrow 4N_2 + 6H_2O, \quad \Delta G^{\circ}_{298} = -1627\ \text{kJ/mol} \qquad (1)$$

A typical commercial catalyst for SCR of NO_x is V_2O_5–WO_3-(MoO_3)/TiO_2 [9,10]. This catalyst is operated at a temperature range of 300–400 °C, and the SCR reactor is located upstream from the particle removal or desulfurizer device to avoid reheating of the flue gas. However, this renders the catalyst more susceptible to deactivation from high concentration of dust (e.g., K_2O, CaO and As_2O_3) and SO_2. Thus, the development of a highly active catalyst for low-temperature SCR (<200 °C) that works downstream of the electrostatic precipitator and desulfurization offers enormous potential, which could also lead to improved economics for the SCR process.

Some transition metal-oxides and mixed-oxide catalysts have been investigated in the low-temperature SCR reaction including Co_3O_4 [11], MnO_x [12], MnO_x/TiO_2 [13], CrO_x/TiO_2 [14], Fe–Mn/TiO_2 [15], CuO_x–MnO_x [16] and MnO_x–CeO_2 [17]. Of all the catalysts screened, Mn-containing catalysts exhibited relatively high activity for the conversion of NO_x. An early report suggested that MnO_x–CeO_2 mixed oxides gave greater than 90% of NO conversion at 100 °C [18]. Sreekanth et al. [19] compared the NO conversions of Cr/TiO_2, Mn/TiO_2, Mn–Cu/TiO_2 and Mn–Cr/TiO_2, and their results showed that Mn/TiO_2 gave the best activity, of about 90% of NO conversion, at 120 °C, whereas TiO_2 supported Mn–Cr/TiO_2 showed a low activity of about 60% NO conversion at 120 °C at a low space velocity ($[NO] = [NH_3] = 2000$ ppm, GHSV = 8000 h^{-1}). In many cases, the activity of redox mixed catalysts is highly dependent on the precise molar ratio used and their method of preparation. In this paper, an extensive study of Cr–MnO_x mixed oxide for low-temperature NO_x reduction with NH_3 is reported. The identification of the present Cr–MnO_x was mainly achieved through the initial screening of 120 mixed oxides prepared by the solid phase synthesis. This combinatorial approach of blending two elements from the given list of Mg, Ti, V, Cr, Mn, Fe, Co, Ni, Cu, Zn, Sr, Zr, Mo, Ba, W and Bi in searching active bimetallic mixed oxides was

* Corresponding author. Fax: +86 20 8711 4707.
** Corresponding author. Fax: +44 186 528 2610.
E-mail addresses: cexhli@scut.edu.cn (X. Li), edman.tsang@chem.ox.ac.uk (S. Chi Tsang).

0021-9517/$ - see front matter © 2010 Elsevier Inc. All rights reserved.
doi:10.1016/j.jcat.2010.08.016

rather empirical and no extensive comparison between them at different testing conditions was carried out. It would be ideal to identify the guiding rules for the selection of active mixed redox oxides. However, the effects of synergy between two or more metal oxides at a close proximity are rather complex and are still not yet clear from the literature. Nevertheless, we noted that the Cr–MnO_x mixed oxides show exceptional SCR activity in our initial evaluation. In this paper, we report various Cr–MnO_x phases that were prepared by the citric acid method and tested for low-temperature SCR activity. The mixed-oxide phase, $CrMn_{1.5}O_4$, was clearly found to be active for low-temperature SCR. The surface area, crystalline phases, ratios of chromium and manganese ions and the promoting effect of $CrMn_{1.5}O_4$ were attributed to different catalytic activities measured for the Cr–MnO_x catalysts. The electron transfer between chromium and manganese with relevance to the mechanism for low-temperature SCR process is discussed.

2. Experimental

2.1. Catalyst preparation

Chromium nitrate, manganese acetate and citric acid were mixed in designated ratios. The mole ratio of citric acid to the metal components (the total moles of chromium and manganese) was set at 1.0. The resulting mixture was stirred at room temperature for 1.0 h. The solution was dried at 120 °C for 12 h, resulting in a porous, foam-like solid. The foam-like precursor was calcined at the desired temperature for 3.0 h in air in a temperature programmed muffle furnace (3–550, Vulcan, USA). Finally, the samples were crushed and sieved to 60–100 mesh. Pure chromium oxide (CrO_x) and manganese oxide (MnO_x) were also prepared using the same procedure; CrO_x–MnO_x was prepared by physically mixing the pure CrO_x and MnO_x with an equal molar ratio of Cr to Mn and then calcined at 650 °C for 3.0 h. The mixed oxide was denoted as Cr(y)–MnO_x(z), where y represented the mole ratio of Cr/(Cr + Mn) and z denoted the calcination temperature in °C, e.g., Cr(0.4)–MnO_x (650).

2.2. Catalyst characterization

A Micromeritics ASAP 2010 micropore-size analyzer was used to measure the N_2 adsorption isotherms of the samples at liquid N_2 temperature (−196 °C). The specific surface area was determined from the linear portion of the BET plot. The pore-size distribution was calculated from the desorption branch of the N_2 adsorption isotherm using the Barrett–Joyner–Halenda (BJH) formula. Prior to the surface area and pore-size distribution measurements, the samples were degassed in vacuum at 300 °C for 24 h.

X-ray diffraction (XRD) patterns were obtained using a Rigaku D/MAX-3A Auto X-ray diffractometer with Cu Kα radiation (λ = 1.5418 Å). Intensity data were collected over a 2θ range of 5–85° with a 0.05° step size and a counting time of 1 s per point. The XRD phases were identified by comparison with the reference data from International Center for Diffraction Data (ICDD) files. A scanning electron microscope (JSM-7401F, JEOL, Japan) was used to obtain surface information on the catalysts.

The TPR experiments were carried out on a Micromeritics AutoChem 2920 chemisorption analyser. A 30 mL min^{-1} (NTP) gas flow of 10% H_2 in Ar was passed over approximately 100 mg samples in a quartz reactor through a cold trap to the detector. The reduction temperature was linearly raised at 10 °C min^{-1} from 30 to 950 °C.

X-ray photoelectron spectroscopy (XPS) analyses were performed using a Quantum-2000 Scanning ESCA Microprobe (Physical Electronics) with a hemispherical detector operating at constant pass energy (PE = 46.95 eV). An X-ray source at 210 W (I = 15 mA, U = 14 kV) and Al Kα radiation (1486.6 eV) were used. The sample powders before or after testing were transferred and pelletized with a diameter of 0.2 mm under an inert atmosphere without exposure to air. They were then examined by the XPS equipment at room temperature. Intensities were estimated from the integration of each peak, after smoothing, subtraction of the L-shaped background, and fitting the experimental curve to a combination of Lorentzian and Gaussian lines of variable proportion. All binding energies were referenced to the C 1s line at 284.6 eV. Binding energy values were measured with a precision of ±0.3 eV.

Raman spectra of materials were taken with a Raman spectrometer (LabRam HR, Horiba Jobin Yvon Inc.) equipped with Olympus BX-41 microscope (objective × 100) and TE-cooled CCD detector (Andor), in a backscattering configuration using He–Ne laser (632.8 nm excitation line) with power of 5–20 mV at a sample and spectral resolution of 0.8 cm^{-1}.

2.3. Catalytic activity measurement

The SCR activity measurement was carried out in a fixed-bed quartz reactor (i.d. = 8 mm). The typical reactant gas composition was as follows: 1000 ppm NO, 1000 ppm NH_3, 3% O_2, and balance N_2 or He (for selectivity experiments). About 3.2 g catalyst (60–100 mesh) was used for each run. Under ambient conditions, the total flow rate was 860 mL min^{-1} and the gas hourly space velocity (GHSV) was 30,000 h^{-1}. The compositions of the feed gases and the effluent streams were monitored continuously using on-line sensors with emission monitors: gas analyzer (SWG-300, MRU, Germany) for NO, NO_2 and SO_2. Without catalyst, it was found that the NO conversion to NO_2 was less than 1%. Thus, the envisaged effect of NO_2 on the SCR activity at such low concentration was not significant. The effluent streams were also analyzed by a gas chromatograph (4890D, HP, USA) at 60 °C with 5 Å molecular sieve column for N_2 and Porapak Q column for N_2O. All data were collected from 10 min to 30 min (steady state) at the chosen temperature. From the concentration of the gases at steady state, the conversion and N_2 selectivity are calculated according to the following equations:

$$NO_x \text{ conversion } (\%) = \frac{[NO_x]_{in} - [NO_x]_{out}}{[NO_x]_{in}} \times 100\% \quad (2)$$

$$N_2 \text{ selectivity } (\%) = \frac{[N_2]_{out}}{[N_2]_{out} + [N_2O]_{out}} \times 100\% \quad (3)$$

where $[NO_x] = [NO] + [NO_2]$, and the subscripts *in* and *out* indicated the inlet and outlet concentration at steady state, respectively. Because the reaction was carried out at low temperature, it was important to ensure that the decrease in NO was not caused by the adsorption of NO by catalyst material. In each experiment, catalyst was purged until the NO concentration reached the expected gas concentration (1000 ppm).

2.4. Normal temperature and pressure plasma reoxidation [20]

A normal pressure electrical glow discharge was used to activate oxygen on catalytic surface in a stream of flowing pure oxygen. The discharge was excited by a 10 MHz RF generator in a silica glass tube with external sleeve electrodes. Typical experimental conditions were a temperature of 25 °C, a pure oxygen flow rate at 50 mL min^{-1} and residence time of 1.2 s, and a 6 h duration of treatment.

2.5. NO oxidation to NO_2

The experiment of NO oxidation to NO_2 was performed in the fixed-bed quartz reactor. Conversion at each temperature was determined using 3.2 g of sample, and 30 min after, steady state

conditions were reached. The reactant gas composition was as follows: 1000 ppm NO, 3% O_2, with the balance N_2; the total flow rate was 860 mL·min^{-1} (ambient conditions). The NO concentration was continually monitored by the above gas analyzer. NO conversion to NO_2 was obtained by Eq. (4):

$$\text{NO conversionto NO}_2\ (\%) = \frac{[NO_2]_{out} - [NO_2]_{in}}{[NO]_{in}} \times 100\% \qquad (4)$$

3. Results and discussion

3.1. Low-temperature activity of CrO_x, MnO_x, CrO_x–MnO_x and Cr(0.5)–MnO_x

The performances of CrO_x, MnO_x, Cr(0.5)–MnO_x catalysts prepared by the citric acid method and mechanically mixed CrO_x–MnO_x catalyst for SCR of NO_x with NH_3 in the presence of excess oxygen are shown in Fig. 1. Pure MnO_x catalyst exhibited a well-defined catalytic activity at the relatively high space velocity of 30,000 h^{-1}, which matched well with a previous report [21]. Pure CrO_x showed negligible activity, while the activity of the physical mixture, CrO_x–MnO_x, was found between CrO_x and MnO_x. Notably, a higher NO_x conversion was obtained using the mixed Cr(0.5)–MnO_x (650) catalyst. This observation clearly implies that the inclusion of Cr into the MnO_x lattice in the mixed oxide (citric acid method), rather than the physical mixing, is the determining factor in the significant gain in activity of the Cr(0.5)–MnO_x catalysts.

Fig. 2 shows the XRD patterns of the above CrO_x, MnO_x, CrO_x–MnO_x and Cr–MnO_x catalysts. CrO_x and MnO_x sample give sharp XRD peaks (Fig. 2a and b) representing Cr_2O_3 (ICDD PDF #84-1616 $2\theta = 33.6°$, 54.9° and 36.3°) and Mn_3O_4 phases (ICDD PDF #89-4837 $2\theta = 36.1°$, 59.9° and 32.3°), respectively. The XRD pattern of CrO_x–MnO_x (Fig. 2c) is consistent with the combination of Cr_2O_3 and Mn_2O_3 phases (ICDD PDF #89-4836 $2\theta = 32.9°$, 55.1° and 65.8°), while a totally new and dominant phase, $CrMn_{1.5}O_4$ (Fig. 2d, ICDD PDF #71-0982 $2\theta = 35.1°$, 61.9° and 29.8°), appears in the Cr(0.5)–MnO_x catalyst. Hence, the superior high activity of the mixed oxide suggested that the generated $CrMn_{1.5}O_4$ phase may be crucially important in the Cr(0.5)–MnO_x catalyst compared to CrO_x, MnO_x and CrO_x–MnO_x.

3.2. Effect of calcination temperature

For the mixed oxides, the calcination temperature is important to provide activation energy to reorganize the mixed materials into a new crystalline phase [22]. Fig. 3 shows the XRD patterns of Cr(0.5)–MnO_x calcined at different temperatures. It is clear that the XRD peaks of all catalysts calcined at various temperatures could all be plausibly attributed to $CrMn_{1.5}O_4$ and the intensities of the XRD peaks were sharper with increasing calcination temperature. The SEM images of Cr(0.5)–MnO_x catalysts calcined at different temperatures are also shown in Fig. 4. All the above phenomena match with the increasing crystallinity of the materials (Fig. 3). Based on the XRD patterns and SEM images, the crystallinity of the materials was found to be significantly improved when the calcination temperature was raised from 550 to 700 °C.

The effect of calcination temperature on the activities of Cr(0.5)–MnO_x mixed-oxide catalysts is shown in Fig. 5. It shows clearly that the SCR activity depends on calcination temperature. NO_x conversions reached nearly 100% on every catalyst at above 140 °C. It is noted that the Cr(0.5)–MnO_x calcined at 650 °C gave the optimum activity at lower temperature. The slight decrease in activity at 700 °C was attributed to lower surface area of the crystalline material due to sintering (Table 1). It was also found that the BET surface areas of the samples continuously decreased upon the increase in calcination temperature, while the conversion first increased before it was dropped to lower values. It should be noted that the BET surface area is not the only parameter affecting activity but also the phase composition. Thus, there must be a complex interplay between surface area and phase composition affect-

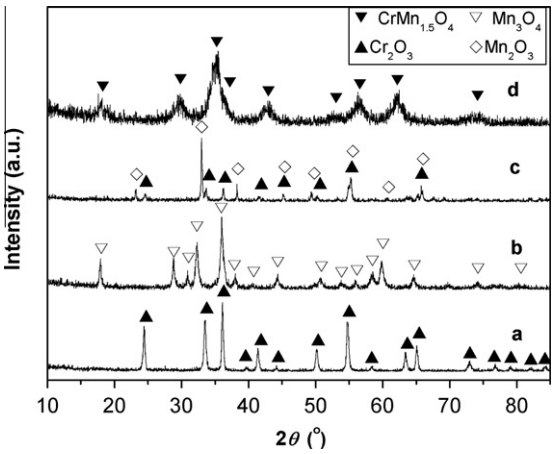

Fig. 2. XRD patterns of CrO_x, MnO_x, CrO_x–MnO_x and Cr–MnO_x catalysts: (a) CrO_x; (b) MnO_x; (c) CrO_x–MnO_x; (d) Cr(0.5)–MnO_x.

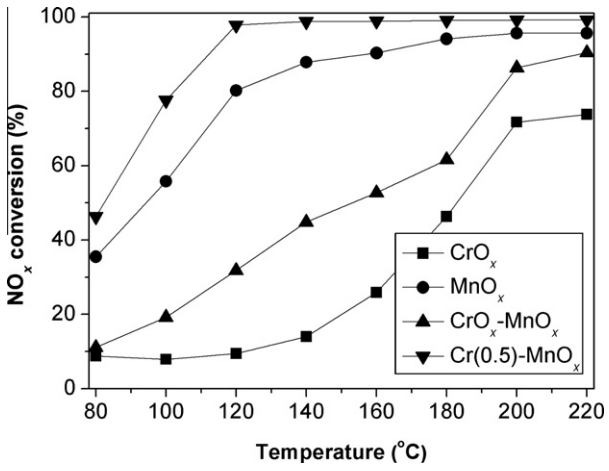

Fig. 1. SCR activity of the CrO_x, MnO_x, CrO_x–MnO_x and Cr(0.5)–MnO_x. Reaction conditions: [NO] = [NH_3] = 1000 ppm, [O_2] = 3%, GHSV = 30,000 h^{-1}, catalysts calcined at 650 °C.

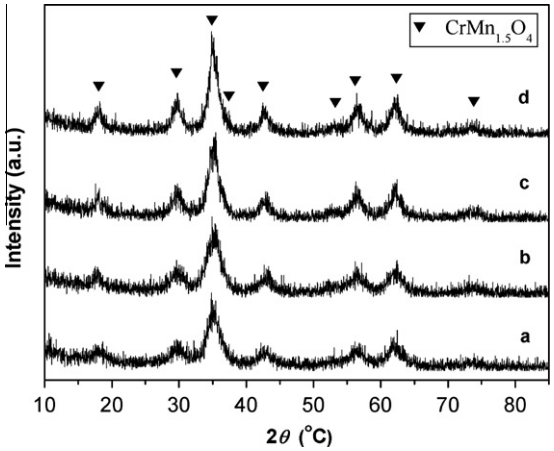

Fig. 3. XRD patterns of the Cr(0.5)–MnO_x mixed-oxide catalysts calcined at different temperatures: (a) 550 °C; (b) 600 °C; (c) 650 °C; (d) 700 °C.

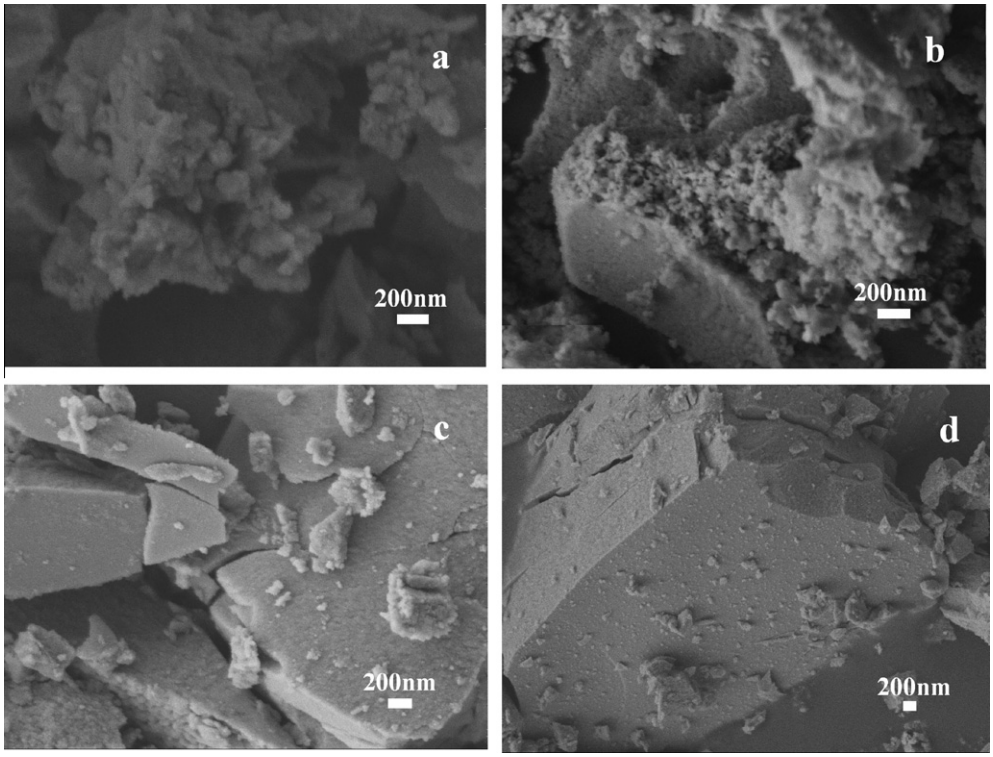

Fig. 4. SEM images of Cr(0.5)–MnO_x calcined at different temperatures: (a) Cr(0.5)–MnO_x(550); (b) Cr(0.5)–MnO_x(600); (c) Cr(0.5)–MnO_x(650); (d) Cr(0.5)–MnO_x(700).

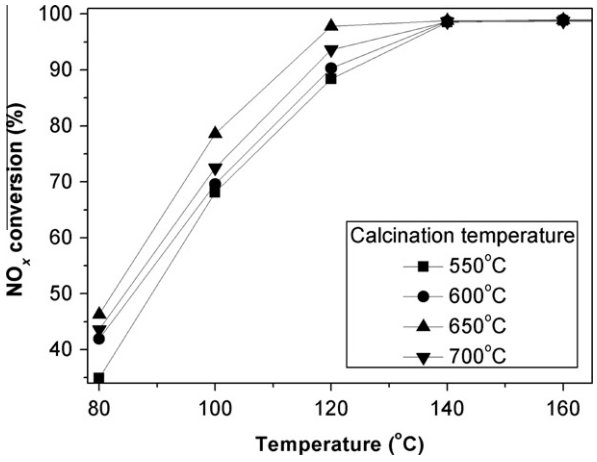

Fig. 5. SCR activity of Cr(0.5)–MnO_x catalyst calcined at different temperatures: Reaction conditions: [NO] = [NH_3] = 1000 ppm, [O_2] = 3%, GHSV = 30,000 h^{-1}.

Table 1
Effect of calcination temperature on surface area and pore characterization.

Entry	Catalysts	BET surface area ($m^2\ g^{-1}$)	Pore volume ($cm^3\ g^{-1}$)	Average pore diameter (nm)
1	Cr(0.5)–MnO_x (550)	65.3	0.046	3.90
2	Cr(0.5)–MnO_x (600)	60.6	0.045	3.83
3	Cr(0.5)–MnO_x (650)	56.1	0.049	3.78
4	Cr(0.5)–MnO_x (700)	40.9	0.045	3.65

ing the present overall activity trend with respect to calcination temperature.

3.3. Effect of the composition of Cr–MnO_x catalyst

A series of Cr–MnO_x catalysts with different molar ratios of Cr/(Cr + Mn) were prepared, calcined at 650 °C and their catalytic performances investigated (Table 2). The data show that NO_x conversion was close to 100% for temperatures above 160 °C for each Cr–MnO_x catalyst. Below 160 °C, there are significant differences in activities among these catalysts: catalytic activity increases with increasing chromium content and the optimum catalytic activity peaked at Cr(0.4)–MnO_x, in which the molar ratio of Cr to Mn is consistent with the stoichiometry of $CrMn_{1.5}O_4$ (Cr:Mn = 2:3). At this ratio, we obtain 80.9% and 98.5% conversions of NO_x at 100 and 120 °C, respectively, at a space velocity of 30,000 h^{-1}. Any further increase in Cr content results in a decline in activity. Fig. 6 shows the XRD patterns of these Cr–MnO_x catalysts. Cr(0.1)–MnO_x could be considered as mixed oxides of Mn_3O_4 and MnO (ICDD PDF #89-4835 $2\theta = 40.6°$, 58.7° and 34.9°), with Mn_3O_4 as the major component. With increasing Cr content, the XRD peak of the $CrMn_{1.5}O_4$ phase increased at the expense of the Mn_3O_4 and MnO phases. For Cr(0.4)–MnO_x, the $CrMn_{1.5}O_4$ phase was dominant with MnO phase also present (Fig. 6d). The Cr(0.5)–MnO_x catalyst gave the same sharp XRD peaks of the $CrMn_{1.5}O_4$ phase (Fig. 6e) as that of Cr(0.4)–MnO_x, but without any evidence of a MnO phase. At this Cr:Mn ratio, we conclude that all the manganese atoms were in the form of $CrMn_{1.5}O_4$. At the same time, no chromic oxide phase was detected by our XRD. From the theoretical viewpoint, the content of the $CrMn_{1.5}O_4$ phase in the Cr(0.4)–MnO_x catalyst would be higher than that of Cr(0.5)–MnO_x, as judged by the stoichiometry of $CrMn_{1.5}O_4$. By inspection of the surface properties of these catalysts (Table 3), the formation of $CrMn_{1.5}O_4$ seemed to be associated with an increase in the surface area of the materials. When the molar ratio of Cr/(Cr + Mn) reached the stoichiometry of the $CrMn_{1.5}O_4$ phase, the pore volume and average pore diameter appeared to decrease. The SEM micrographs of Cr–MnO_x catalysts (Fig. 7) clearly reflected the phase change with the increasing content of Cr. For

Table 2
NO_x conversions of various Cr–MnO_x catalysts doped at differing Cr levels.[a]

Catalysts	NO_x conversion (%)							
	80 °C	100 °C	120 °C	140 °C	160 °C	180 °C	200 °C	220 °C
Cr(0.1)–MnO_x	31.8	52.7	79.1	94.6	98.5	98.7	98.8	98.8
Cr(0.2)–MnO_x	35.1	59.7	88.0	98.4	98.8	99.0	99.0	99.0
Cr(0.3)–MnO_x	45.9	74.8	97.1	98.8	98.9	99.1	99.2	99.2
Cr(0.4)–MnO_x	48.5	80.9	98.5	99.2	99.5	99.7	99.7	99.7
Cr(0.5)–MnO_x	46.3	77.6	97.8	98.8	98.9	99.0	99.1	99.1

[a] Reaction conditions: [NO] = [NH_3] = 1000 ppm, [O_2] = 3%, GHSV=30,000 h^{-1}

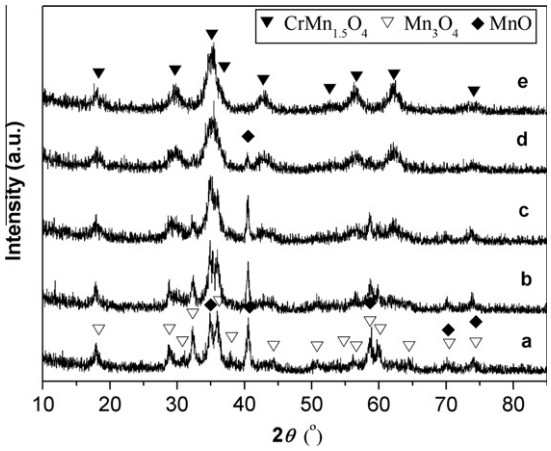

Fig. 6. XRD patterns of the Cr–MnO_x catalysts doped at a range of Cr content: (a) Cr(0.1)–MnO_x; (b) Cr(0.2)–MnO_x; (c) Cr(0.3)–MnO_x; (d) Cr(0.4)–MnO_x; (e) Cr(0.5)–MnO_x.

Table 3
Surface area and pore characterization of catalysts.

Entry	Catalysts	BET surface area ($m^2\ g^{-1}$)	Pore volume ($cm^3\ g^{-1}$)	Average pore diameter (nm)
1	CrO_x (650)	29.9	0.127	14.1
2	MnO_x (650)	19.2	0.112	21.2
3	CrO_x–MnO_x (650)	22.6	0.108	16.9
4	Cr(0.1)–MnO_x (650)	60.4	0.097	11.0
5	Cr(0.2)–MnO_x (650)	66.5	0.097	13.0
6	Cr(0.3)–MnO_x (650)	86.8	0.082	7.80
7	Cr(0.4)–MnO_x (650)	70.4	0.053	4.52
8	Cr(0.5)–MnO_x (650)	56.1	0.049	3.78

example, Cr(0.1)–MnO_x was composed mainly of small particles of an amorphous phase (Fig. 7a), while a more crystalline phase appeared in the Cr(0.2)–MnO_x; at this point, the microcrystalline component increased and became dominant with the increase in Cr, which also matched well with the results of XRD characterization (Fig. 6).

3.4. Lifetime study and SO_2 resistance of Cr(0.4)–MnO_x

As the above, Cr(0.4)–MnO_x catalyst showed very good NO_x SCR activity, its lifetime and regeneration properties were investigated. The catalyst was first operated for 500 h and then generated by normal temperature and pressure plasma. Experimental results (Fig. 8) showed that the initial SCR activity of Cr(0.4)–MnO_x was very high (NO_x conversion at 99%) and still remained at 91.7% with 100% N_2 selectivity after 500 h of a continuous lifetime test. This catalyst can be reactivated easily, as NO_x conversion was recovered to the same level comparable to a fresh sample, with the selectivity still maintained at 100% after regeneration. This clearly suggests that the Cr(0.4)–MnO_x displays a satisfactory degree of stability and regeneration properties in our laboratory scale work.

It is difficult to remove all of the SO_x after any desulfurization process, and thus, traces of SO_2 may still exist (usually about 100 ppm) and affect the denitrogen catalysis downstream. The SO_2 resistance of the Cr(0.4)–MnO_x(650) catalysts was therefore taken into consideration in comparison with that of MnO_x(650) (Fig. 8). It indicates that the NO_x conversion on Cr(0.4)–MnO_x decreases slowly, losing 15% of its activity in 4 h when 100 ppm SO_2 was added to the reaction gas stream under 120 °C with a total space velocity of 30,000 h^{-1}. Nevertheless, it still shows a very high level of activity for NO_x conversion. Interestingly, the activity was rapidly restored to 96% when the SO_2 flow was stopped. However, the NO_x conversion on MnO_x decreases sharply, and most of its activity (about 84%) is lost in 4 h only 50% of its original activity could be restored, while SO_2 was stopped. It can be concluded that this new Cr(0.4)–MnO_x catalyst maintains a good de-NO_x activity in a high sulfur content gas stream. Although the sulfur-tolerance of the Cr(0.4)–MnO_x catalyst needs to be improved, its low-temperature SCR activity was much higher than the MnO_x catalyst in the presence of SO_2. It should be cautious to note that these experiments were conducted in the short time exposure of SO_2. The effects of continuous feeding SO_2 at prolonged period of time were not studied. In addition, the present results were obtained from using our small-scale laboratory testing and the industrial applicability of our new catalysts is not yet known at this stage.

3.5. H_2-TPR analysis

The H_2-TPR patterns of the catalysts are shown in Fig. 9. CrO_x is reduced at 233 °C due to the reduction of Cr_2O_3 to CrO [23,24]; MnO_x shows two stages of reduction at 187 and 439 °C, respectively, and Mn_2O_3 reduction to Mn_3O_4 followed by Mn_3O_4 reduction to MnO [25]. The TPR profile of CrO_x–MnO_x is that of the combination of two physically mixed oxides, but interaction between CrO_x and MnO_x is also evident, as the reduction temperature of MnO_x in CrO_x–MnO_x is clearly shifted to lower temperature and that of CrO_x in CrO_x–MnO_x to higher temperature. Both Cr(0.4)–MnO_x and Cr(0.5)–MnO_x mixed-oxide catalysts, on the other hand, show nearly the same reduction behaviors, which are quite different from those of pure oxides. With comparison with pure oxides and combined with the fact that the reduction peak around 240 °C increases with the increasing Cr content, peak temperatures around 240 and 340 °C can be attributed to the reduction of Cr–O bonds and Mn–O bonds in $CrMn_{1.5}O_4$ phases, respectively. Nevertheless, the reduction of the mixed-oxide phase was clearly facilitated by the significant peak shift; for example, the reduction temperature of Cr–O bonds is a little higher than that of CrO_x, while

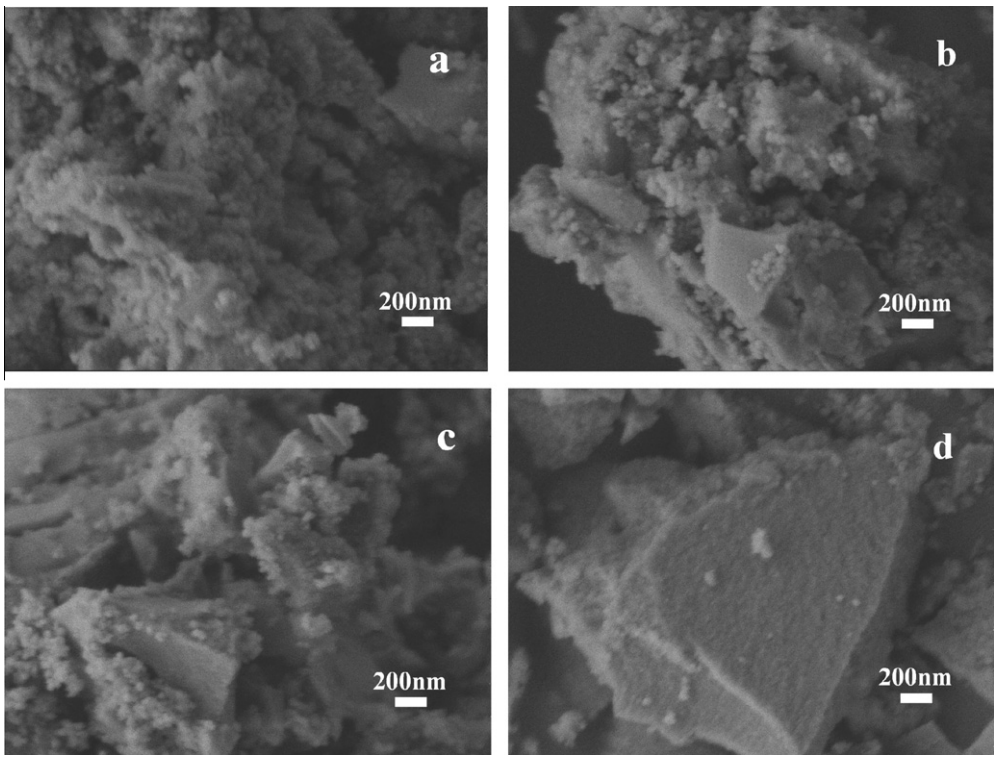

Fig. 7. SEM images of the catalysts: (a) Cr(0.1)–MnO_x(650); (b) Cr(0.2)–MnO_x(650); (c) Cr(0.3)–MnO_x(650); (d) Cr(0.4)–MnO_x(650).

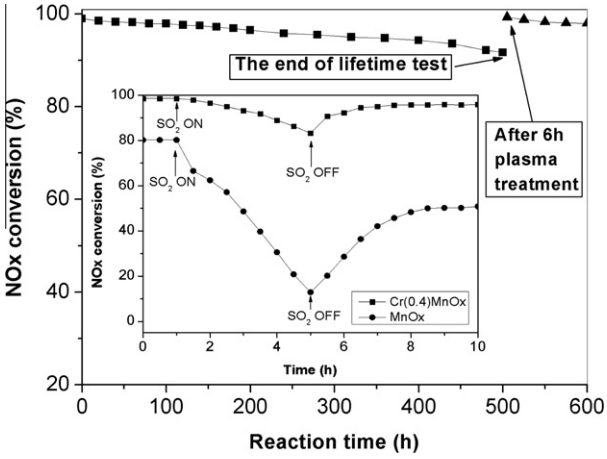

Fig. 8. Lifetime and sulfur-tolerance study of Cr(0.4)–MnO_x catalyst at 120 °C. Reaction conditions: [NO] = [NH_3] = 1000 ppm, [O_2] = 3%, [SO_2] = 100 ppm, GHSV = 30,000 h^{-1}.

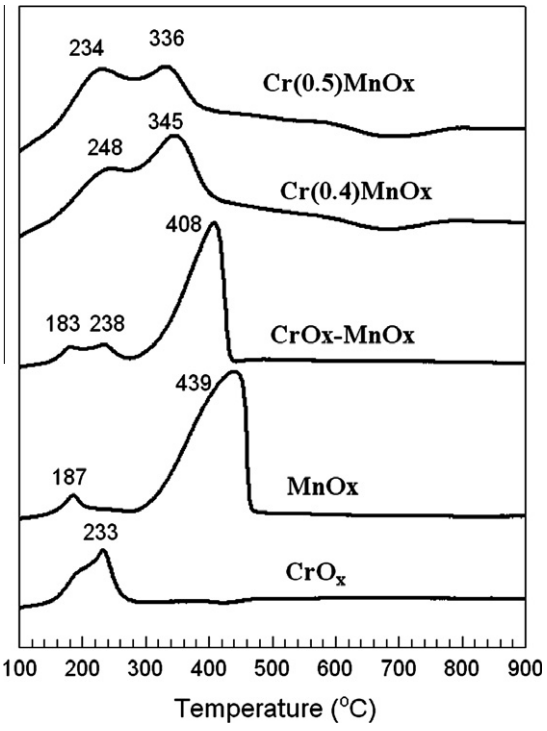

Fig. 9. TPR profiles of the catalyst samples.

the reduction temperature of Mn–O bonds is at least 100 °C lower than that of MnO_x.

According to the ICDD, Mn_3O_4 has a body-centered tetragonal structure, Cr_2O_3 is hexagonal and $CrMn_{1.5}O_4$ is face-centered cubic. The crystalline structures of Mn_3O_4, MnO, Cr_2O_3 and $CrMn_{1.5}O_4$ are shown in Fig. 10, and the lengths of all metal–oxygen bonds are compiled in Table 4. There are three different types of Mn–O bonds in Mn_3O_4 (MnO_x), with bond lengths of 2.0142, 1.9475 and 2.2922 Å. Two types of Cr–O bond exist in the Cr_2O_3 (CrO_x) with bond lengths of 2.0367 and 1.9458 Å. As for the unit cell of $CrMn_{1.5}O_4$, we can see that metal atoms (Cr or Mn) are connected through oxygen atoms in the form of Cr(Mn)–O–Mn in the $CrMn_{1.5}O_4$ lattice. The interatomic connections are mainly in the form of Cr–O–Mn and Mn–O–Mn, the Cr atom is connected tetrahedrally to four oxygen atoms, while the Mn atom is connected octahedrally to six oxygen atoms. It is noted that in the $CrMn_{1.5}O_4$ lattice, the length of the Mn–O bond (2.3509 Å) is greater than that of the Mn–O bonds in MnO_x, but that the bond length of the Cr–O bond (1.4686 Å) is less than those of the Cr–O bonds in CrO_x.

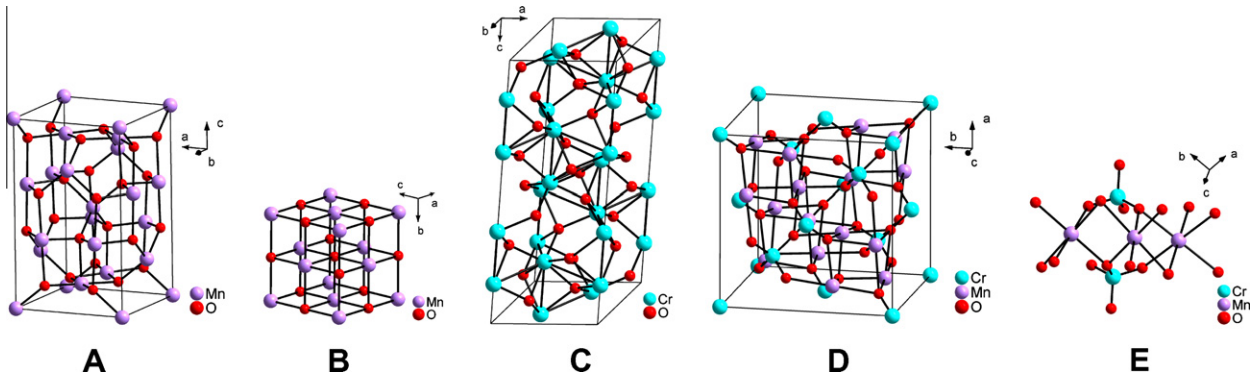

Fig. 10. Structures of Mn_3O_4, MnO, Cr_2O_3, $CrMn_{1.5}O_4$ crystalline and $CrMn_{1.5}O_4$ unit cell: (A) Mn_3O_4; (B) MnO; (C) Cr_2O_3; (D) $CrMn_{1.5}O_4$; (E) $CrMn_{1.5}O_4$ unit cell. Purple ball: Mn; Red ball: O; blue ball: Cr. (For interpretation of the references to colour in this figure legend, the reader is referred to the web version of this article.).

Table 4
M–O bond lengths in the manganese–chromium–oxide system.

Crystal phase	Bond	Bond length (Å)
Mn_3O_4	Mn–O	2.2922
	Mn–O	1.9475
	Mn–O	2.0142
MnO	Mn–O	2.2215
Cr_2O_3	Cr–O	2.0367
	Cr–O	1.9458
$CrMn_{1.5}O_4$	Mn–O	2.3509
	Cr–O	1.4686

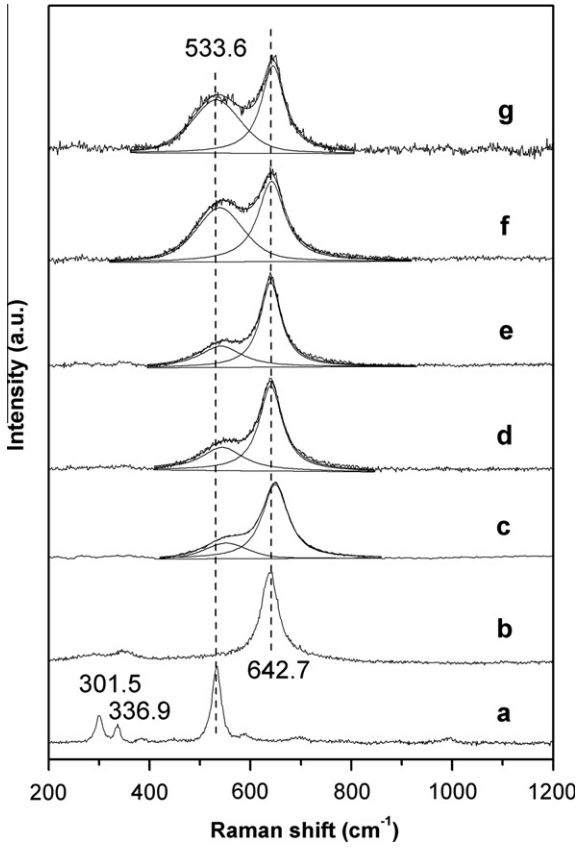

Fig. 11. Raman spectra of catalysts. (a) CrO_x; (b) MnO_x; (c) Cr(0.1)–MnO_x; (d) Cr(0.2)–MnO_x; (e) Cr(0.3)–MnO_x; (f) Cr(0.4)–MnO_x; (g) Cr(0.5)–MnO_x. Crude line: original data; Smooth line: fitting line.

It had been established in the literature that a shift in the peak position of the reduction temperature can be attributed to many factors, such as change in particle size, lattice oxygen mobility, phase composition or structural defects [26]. The change in reduction temperature also reflects the variation in reduction potential of oxidized metallic species in $CrMn_{1.5}O_4$ by comparison with those of corresponding monometallic oxide catalysts. The above TPR patterns clearly reflect the changes in the chemical environments of Mn and Cr (i.e. bond energy change); for example, the reduction temperature of manganese in $CrMn_{1.5}O_4$ is lower than that of pure MnO_x owing to the longer Mn–O distance, and similarly the increase in reduction temperature of chromium with respect to that of CrO_x reflects the shortening of the Cr–O bond.

3.6. Analysis of Raman spectra

The Raman spectra of pure CrO_x, MnO_x and Cr–MnO_x catalysts are shown in Fig. 11, and their detailed Raman shifts are listed in Table 5. The spectrum of CrO_x shows three Raman bands peaked at 301.5, 336.9 and 533.6 cm^{-1} (Fig. 11a). These bands are attributed to Cr_2O_3 [27–29]. For MnO_x, the broad Raman shift peak at 642.7 cm^{-1} (Fig. 11b) is characteristic of Mn_3O_4 [30,31] and represents the single Mn–O bond vibration. These results were in agreement with pure chromium and magnesium oxide phases detected by XRD (Fig. 2). Although the characteristic Raman band of the Mn–O bond in MnO lies at 537 cm^{-1} [32], it may not be detected by this technique, as MnO can be easily transformed to Mn_3O_4 under a laser beam [33].

It can be seen from Fig. 11 that the Raman peak at around 540 and 640 cm^{-1} increases in intensity with increasing Cr content. Hence, these bands can be assigned to the Raman shift of Cr–O and Mn–O bond in the form of Cr–O–Mn, respectively, as the $CrMn_{1.5}O_4$ phase increases with the increasing of Cr content proved by the XRD data (Fig. 6) and SEM observations (Fig. 7). These peaks are quite different from those of pure CrO_x and MnO_x (533.6 and 642.7 cm^{-1}, respectively). The changes in crystal structure and in the bond lengths are responsible for the shifts of the Raman peaks [34]. For example, not only the peaks at 301.5, and 336.9 cm^{-1} (attributed to CrO_x) disappeared, but also another sharp Raman band due to CrO_x (located at 533.6 cm^{-1}) was replaced by a flat peak around 539–549 cm^{-1}. This wavenumber shift could be attributed to a decrease in the bond length of Cr–O in $CrMn_{1.5}O_4$ relative to those of CrO_x (Table 4); Accordingly, the Raman shift of the Mn–O bond in the mixed oxide is found at lower wavenumber than that of Mn–O in MnO_x as the length of Mn–O in $CrMn_{1.5}O_4$ is longer (than that in MnO_x; Table 4). When the Cr content exceeded the stoichiometry of the $CrMn_{1.5}O_4$ phase (for Cr(0.5)–MnO_x, Table 5, entry 7), the Raman spectra reflected the mixture

Table 5
Raman shift data of oxide catalysts.

Entry	Catalysts	Raman shift (cm^{-1})	
		Cr–O	Mn–O
1	CrO_x	533.6	–
2	MnO_x	–	642.7
3	Cr(0.1)–MnO_x(650)	549.1	646.1
4	Cr(0.2)–MnO_x(650)	544.2	640.3
5	Cr(0.3)–MnO_x(650)	541.1	640.1
6	Cr(0.4)–MnO_x(650)	539.3	641.7
7	Cr(0.5)–MnO_x(650)	532.5	644.6

of Cr–O bonds (in the form of CrO_x) and Cr–O–Mn (in the form of $CrMn_{1.5}O_4$). Hence, the variations of the structure and chemical state of the mixed catalyst are readily shown by this Raman investigation, which also matches well with the above characterization and theoretical considerations. For Cr(0.4)–MnO_x, the molar ratio of Cr to Mn is equal to the stoichiometry of $CrMn_{1.5}O_4$ phase, and this phase is perfect and stable with a large number of Cr(Mn)–O–Mn bonds (Fig. 10); therefore, we could draw a conclusion that the maxima at 539.3 and 641.7 cm^{-1} can be assigned as Raman bands of Cr–O and Mn–O bonds in the form of Cr(Mn)–O–Mn respectively. Furthermore, bands of Cr^{6+} in chromium oxide were confirmed to be in the range 800–1000 cm^{-1} [35,36], which were not observed in our patterns. It is well known that there are many other parameters (sample homogeneity, size of crystalline phase, purity, etc.) that affect the Raman shift value. It should be cautious that there is no simple linearity relationship with respect to increasing Cr content.

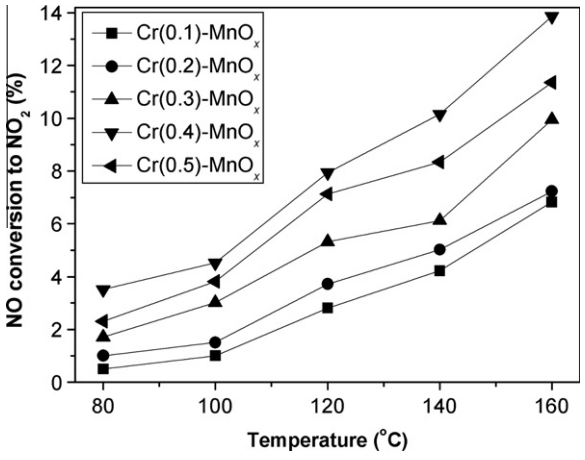

Fig. 12. Oxidation activity of NO to NO_2 on Cr–MnOx catalysts. Reaction conditions: [NO] = 1000 ppm, [O_2] = 3%, and GHSV = 30,000 h^{-1}.

3.7. Oxidation activities of NO to NO_2 on $CrMn_{1.5}O_4$

From above results, the most active catalyst for low-temperature NO_x reduction with NH_3 should be the $CrMn_{1.5}O_4$ phase with suitable surface properties. The in-depth investigation of the oxidation activities of NO to NO_2 on catalysts doped with various ratios of Cr/(Cr + Mn) at 80–160 °C are shown in Fig. 12. With increase of chromium in the Cr–MnO_x catalysts, the NO oxidation activity improved significantly and reached its maximum with Cr(0.4)–MnO_x. The direct catalytic reaction of NO and NH_3 to N_2 is thought to be difficult and it is well known that ammonium nitrite decomposes quickly to give N_2 below 100 °C [37]. The formation of NH_4NO_2 from NO, O_2 and NH_3 requires a prior oxidation of NO to NO_2 by O_2. A highly active catalyst for the oxidation of NO to NO_2 at low temperature, which also gave enhanced SCR activities, has been reported [38,39]. We propose that the beneficial effect of chromium incorporation in Mn as $CrMn_{1.5}O_4$ is because this phase could oxidize NO to NO_2 at low temperatures, thereby enhancing the SCR activity. In addition, it is interesting to observe that the oxidation of NO to NO_2 conversion (Fig. 12) is at least 10 times lower than the NO conversion during SCR process (Table 2). It is now widely accepted that the SCR efficiency can be significantly improved with increasing NO_2 amount due to a faster reaction rate between NO_2 and adsorbed NH_3 [40]. It is also believed that in the SCR process, the presence of the adsorbed NH_3 can continuously mob up the adsorbed NO_2, in situ formed from NO oxidation on catalytic surface. This would dramatically speed up the NO to NO_2 conversion when compared to the pure NO oxidation.

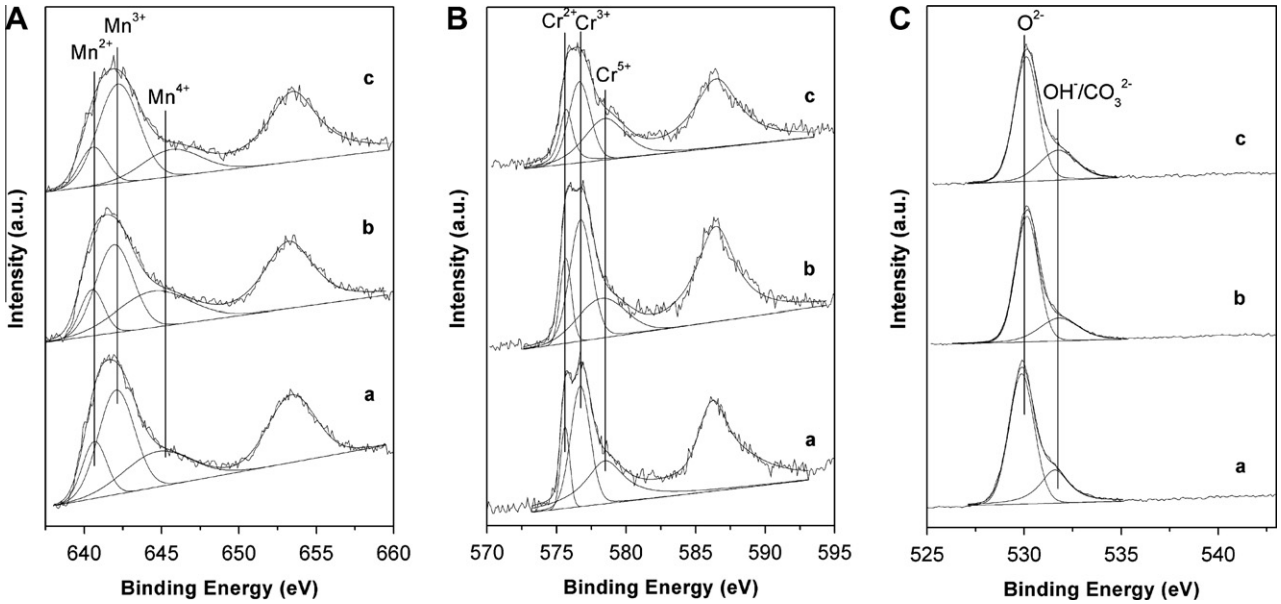

Fig. 13. XPS spectra for (A) Mn 2p, (B) Cr 2p, and (C) O 1s of the Cr(0.4)–MnO_x catalysts. (a) Fresh catalyst; (b) used catalyst; (c) regenerated catalyst.

3.8. XPS analysis and a possible redox reaction over $CrMn_{1.5}O_4$

To investigate the surface chemical states of the most active catalyst, the XPS spectra of the Mn $2p_{3/2}$, Cr $2p_{3/2}$ and O 1s in *fresh*, *used* (catalyst quenched from 500 h operation) and *regenerated* Cr(0.4)–MnO_x(650) catalyst (catalyst operated 500 h and then treated by plasma before quenched for analysis) were obtained, as shown in Fig. 13. Two main peaks due to Mn $2p_{3/2}$ (peak at 643 eV) and Mn $2p_{1/2}$ (peak at 653 eV) were observed (Fig. 13A). The measured binding energies of Mn $2p_{3/2}$ in Cr(0.4)–MnO_x(650) catalyst (640∼645 eV) were slightly higher than those reported for MnO, Mn_2O_3 and MnO_2 [41], which shows a nice distinction in the change in chemical environment between the $CrMn_{1.5}O_4$ phase and single MnO_x, and also fits well with the result discussed above. By performing a peak-fitting deconvolution, the Mn $2p_{3/2}$ spectra can be separated into three peaks: 640.4–640.5, 641.9–642.2 and 644.5–644.8 eV, respectively. There are quite close to the previously reported $Mn2p_{3/2}$ binding energies of Mn^{2+}, Mn^{3+} and Mn^{4+} in MnO_x–CeO_2 mixed oxides with 640.3–640.7, 641.6–642.3 and 643.2–644.5 eV, respectively [42]. The Cr $2p_{3/2}$ of Cr(0.4)–MnO_x(650) catalyst was separated into two peaks by the same peak-fitting deconvolution technique. The "low valence" Cr^{LV} occurred at about 576 eV and the "high valence" Cr^{HV} was characterized by an average binding energy of about 578.3–578.5 eV. The former peaks can be assigned to Cr^{2+} (575.6–575.7 eV) and Cr^{3+} (576.6–576.7 eV) [43,44]. The second peak (578.3–578.5 eV) should be assigned to a higher valence chromium state, perhaps Cr^{5+} or Cr^{6+}. It has been reported that binding energy of Cr^{5+} has a value in the range 578.0–578.8 eV [45,46], and hence, peaks with high oxidation state in the range of 578.3–578.5 eV could be assigned to Cr^{5+} (Fig. 13B). It has also been reported that compounds containing Cr^{6+} exhibited a higher XPS band energy, at 579–580 eV [47,48], which we did not observe. Together with the above Raman shift analysis (Fig. 11), we conclude that the chromium oxidation state in the Cr(0.4)–MnO_x(650) catalyst is mainly Cr^{5+} rather than Cr^{6+}.

Table 6 lists the atom percentage of catalysts determined by XPS. The value of Cr/(Cr + Mn) characterized by XPS was higher than the overall molar ratio of Cr(0.1)–MnO_x and Cr(0.2)–MnO_x and similar to Cr(0.2)–MnO_x, and Cr(0.3)–MnO_x, but lower than overall molar ratio for Cr(0.4)–MnO_x and Cr(0.5)–MnO_x. Notably, the concentration of manganese on the surface of the Cr(0.4)–MnO_x catalyst reached a constant value. The formation of $CrMn_{1.5}O_4$ would account for this. As shown in Fig. 13C, an asymmetric peak was observed in the XPS spectra of O 1s for both fresh, used and regenerated samples. The peak at 529.6–530.0 eV corresponds to lattice oxygen (O^{2-}) whereas the one at 531.3–531.7 eV corresponds to several O_{1s} states assigned to the surface-adsorbed oxygen such as O_2^{2-} or O^-, in the form of hydroxyl, OH^- and carbonate, CO_3^{2-} [49]. Values of Cr/(Cr + Mn) on the surface of used and regenerated catalysts are higher than that of fresh catalyst, which implies that chromic oxide tends to migrate to the surface.

Table 6
Atom percentage of catalysts determined by XPS.

Catalyst	Cr (%)	Mn (%)	O (%)	Cr/(Cr + Mn)
Cr(0.1)–MnO_x	3.5	21.0	75.5	0.14
Cr(0.2)–MnO_x	3.6	13.6	82.8	0.21
Cr(0.3)–MnO_x	4.6	11.4	84.0	0.29
Cr(0.4)–MnO_x	10.9	20.3	68.8	0.35
Cr(0.5)–MnO_x	12.8	17.2	70.0	0.43
Cr(0.4)–MnO_x (*used*)	14.2	21.0	64.8	0.40
Cr(0.4)–MnO_x (*regenerated*)	13.7	18.6	66.7	0.42

The binding energies (eV) of Mn, Cr and O of Cr(0.4)–MnO_x before testing (fresh) and after testing (used) and plasma regeneration (regenerated) are shown in Table 7. It was found that the relative surface concentration of the three species did not change much, but that their relative oxidation states varied significantly. After 500 h of SCR reaction, the concentrations of relatively lower valence state chromium ions (Cr^{2+} and Cr^{3+}) increased at the expense of higher valence state chromium (Cr^{5+}), but the higher valence manganese state (Mn^{4+}) increased, while Mn^{3+} decreased. Plasma treatment of the spent catalysts has the advantage of not changing the structure and morphological properties. It can be seen that the relative high surface concentrations of Mn^{3+} and Cr^{5+} recovered matching with the recovery in the activity of Cr(0.4)–MnO_x. So, the above partial loss in activity of catalyst after 500 h of life test might be due to the decline in Mn^{3+} and Cr^{5+} surface concentrations. Hence, it can be concluded that both Mn^{3+} and Cr^{5+} must play an important role in this SCR process.

To summarize, we observe (1) changes in oxidation states of Mn and Cr after 500 h of operation and also after plasma generation;

Table 7
Binding energies (eV) of core electrons of Cr(0.4)–MnO_x and the percent of differential valence state.[a]

XPS spectra	Element valence	Binding energies (percent of valence state, %)		
		Fresh catalyst	Used catalyst	Regenerated catalyst
Cr 2p (eV) concentration (%)	Cr^{2+}	575.6 (13.9)	575.7 (16.8)	575.7 (19.7)
	Cr^{3+}	576.7 (42.2)	576.7 (49.9)	576.6 (38.0)
	Cr^{5+}	578.4 (43.9)	578.3 (33.3)	578.5 (42.3)
Mn 2p (eV) concentration (%)	Mn^{2+}	640.4 (14.6)	640.5 (15.5)	640.5 (16.0)
	Mn^{3+}	641.9 (54.2)	641.9 (46.9)	642.2 (60.6)
	Mn^{4+}	644.6 (31.2)	644.5 (37.6)	644.8 (23.4)
O 1s (eV) concentration (%)	O^{2-}	529.8 (71.0)	529.8 (73.9)	529.9 (72.2)
	OH^-/CO_3^{2-}	531.6 (29.0)	531.7 (26.1)	531.8 (27.8)

[a] Surface concentration of different Mn, Cr and O states are in parenthesis.

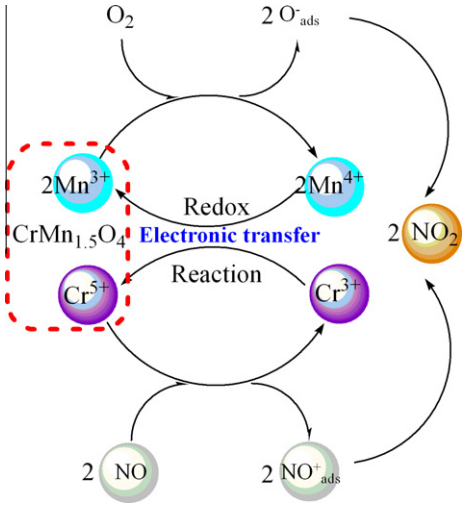

Scheme 1. A redox catalytic cycle of the low-temperature SCR reactions over Cr(0.4)–MnO_x catalysts.

(2) apparent gain of electrons by Cr and loss by Mn in the quenched samples (3) that the concentration of O^{2-} changes little (Table 6) after 500 h of operation and regeneration. We therefore propose electron transfer between Cr and Mn ions. For the $CrMn_{1.5}O_4$ phase, most of the Cr and Mn species are interconnected in the form of Cr–O–Mn through oxygen bridges, facilitating electron transfer. A redox electron transfer between different ions (from Mn^{3+} and Cr^{5+}) through the oxygen bridge (Eq. (5)) is probably similar to the electron transfer between copper and manganese in the $CuMn_2O_4$ system, previously described [16,20,50]. Thus, we propose a redox cycle for low-temperature SCR over this new type of catalysts as depicted in Scheme 1.

$$Cr^{5+} + 2Mn^{3+} \rightarrow Cr^{3+} + 2Mn^{4+} \quad (5)$$

4. Conclusions

Novel Cr–Mn mixed oxides with high activity for the low-temperature SCR of NO_x with ammonia in the presence of oxygen were developed. Greater than 98.5% of NO_x conversion was obtained over the Cr(0.4)–MnO_x (650) catalyst, prepared by the citric acid method at 120 °C, under flow conditions of GHSV = 30,000 h^{-1}. From the XRD patterns, the spinel $CrMn_{1.5}O_4$ was found to be present in active Cr–Mn mixed-oxides catalysts. The TPR profiles are revealed *for the first time* the reduction process of $CrMn_{1.5}O_4$ and the existence of the $CrMn_{1.5}O_4$ phase clearly depressed the reduction temperature of manganese oxides. Raman peaks at around 539.3 and 641.7 cm^{-1} can be assigned to the characteristic Raman bands of the $CrMn_{1.5}O_4$ lattice phase, a new phase to the best of our knowledge. Better oxidation of NO could be ascribed to the formation of $CrMn_{1.5}O_4$, with confirmation of electron transfer between chromium and manganese by XPS. The addition of SO_2 in the feeder gas could exert an adverse effect on the NO_x conversion, but does not seem to create permanent structural alteration to the Mn species (totally reversible sulfur poisoning), presumably due to the existence of high redox potential pairs of Cr and Mn in the structure, permitting efficient regeneration.

Acknowledgment

The National Natural Science Foundation of China (20876063) is gratefully acknowledged for the financial support of this work.

References

[1] H. Schneider, U. Scharf, A. Wokaun, A. Baiker, J. Catal. 147 (1994) 545.
[2] A. Tomita, T. Yoshii, S. Teranishi, M. Nagao, T. Hibino, J. Catal. 247 (2007) 137.
[3] Y. Li, H. Cheng, D. Li, Y. Qin, Y. Xie, S. Wang, Chem. Commun. 12 (2008) 1470.
[4] X. Li, P. Zhu, F. Wang, L. Wang, S.C. Tsang, J. Phys. Chem. C 112 (2008) 3376.
[5] P.J. Smeets, M.H. Groothaert, R.M. Teeffelen, H. Leeman, E.J.M. Hensen, R.A. Schoonheydt, J. Catal. 245 (2007) 358.
[6] J. Zhu, D. Xiao, J. Li, X. Yang, Y. Wu, J. Mol. Catal. A 234 (2005) 99.
[7] J.V. Durme, J. Dewulf, C. Leys, H.V. Langenhove, Appl. Catal. B 78 (2008) 324.
[8] J.L. Hueso, J. Cotrino, A. Caballero, J.P. Espinós, A.R. González-Elipe, J. Catal. 247 (2007) 288.
[9] G.L. Bauerle, S.C. Wu, K. Nobe, Ind. Eng. Chem. Prod. Res. Dev. 14 (1975) 268.
[10] V.M. Mastikhin, V.V. Terkikh, O.B. Lapina, O.B. Filimonova, M. Seial, H. Knözinger, J. Catal. 156 (1995) 1.
[11] R. Ke, J. Li, X. Liang, J. Hao, Catal. Commun. 8 (2007) 2096.
[12] M. Kang, E.D. Park, J.M. Kim, J.E. Yie, Appl. Catal. A 327 (2007) 261.
[13] Z. Wu, B. Jiang, Y. Liu, Appl. Catal. B 79 (2008) 347.
[14] P.G. Smirniotis, D.A. Peña, B.S. Uphade, Angew. Chem. Int. Ed. 40 (2001) 2479.
[15] G. Qi, R.T. Yang, Appl. Catal. B 44 (2003) 217.
[16] M. Kang, E.D. Park, J.M. Kim, J.E. Yie, Catal. Today 111 (2006) 236.
[17] X. Tang, Y. Li, X. Huang, Y. Xu, H. Zhu, J. Wang, W. Shen, Appl. Catal. B 62 (2006) 265.
[18] G. Qi, R.T. Yang, Chem. Commun. 7 (2003) 848.
[19] P.M. Sreekanth, D.A. Peña, P.G. Smirniotis, Ind. Eng. Chem. Res. 45 (2006) 6444.
[20] S. Vepřek, D.L. Cocke, S. Kehl, H.R. Oswald, J. Catal. 100 (1986) 250.
[21] X.L. Tang, J.M. Hao, W.G. Xu, J.H. Li, Chin. J. Catal. 27 (2006) 843.
[22] D.A. Peña, B.S. Uphade, P.G. Smirniotis, J. Catal. 221 (2004) 421.
[23] A. Hakuli, M.E. Harlin, L.B. Backman, A.O.I. Krause, J. Catal. 184 (1999) 349.
[24] B. Grzybowska, J. Słoczyński, R. Grabowski, K. Wcisło, A. Kozłowska, J. Stoch, J. Zieliński, J. Catal. 178 (1998) 687.
[25] S. PalDey, S. Gedevanishvili, W. Zhang, F. Rasouli, Appl. Catal. B 56 (2005) 241.
[26] S. Bhatia, J. Beltramini, D.D. Do, Catal. Today 7 (1990) 309.
[27] A.Y. Kuznetsov, J.S. Almeida, L. Dubrovinsky, R. Ahuja, S.K. Kwon, I. Kantor, N. Guignot, J. Appl. Phys. 99 (2006) 053909.
[28] D. Stanoi, G. Socol, C. Grigorescu, F. Guinneton, O. Monnereau, L. Tortet, T. Zhang, I.N. Mihailescu, Mater. Sci. Eng. B 118 (2005) 74.
[29] H.C. Barshilia, N. Selvakumar, K.S. Rajam, J. Appl. Phys. 103 (2008) 023507.
[30] M. Ludvigsson, J. Lindgren, J. Tegenfeldt, J. Mater. Chem. 11 (2001) 1269.
[31] F. Kapteijn, A.D. Langeveld, J.A. Moulijn, A. Andreïni, M.A. Vuurman, A.M. Turek, J. Jehng, I.E. Wachs, J. Catal. 150 (1994) 94.
[32] H.-H. Chou, H.Y. Fan, Phys. Rev. B 13 (1976) 3924.
[33] F. Buciuman, F. Patcas, R. Craciun, D.R.T. Zahn, Phys. Chem. Chem. Phys. 1 (1999) 185.
[34] H. Wan, D. Li, H. Zhu, Y. Zhang, L. Dong, Y. Hu, B. Liu, K. Sun, L. Dong, Y. Chen, J. Colloid Interface Sci. 326 (2008) 28.
[35] S. Gómez, L.J. Garces, J. Villegas, R. Ghosh, O. Giraldo, S.L. Suib, J. Catal. 233 (2005) 60.
[36] Y. Han, F. Chen, Z. Zhong, K. Ramesh, L. Chen, E. Widjaja, J. Phys. Chem. B 110 (2006) 24450.
[37] F. Notoya, C. Su, E. Sasako, S. Nojima, Ind. Eng. Chem. Res. 40 (2001) 3732.
[38] M. Koebel, M. Elsener, G. Madia, Ind. Eng. Chem. Res. 40 (2001) 52.
[39] R.Q. Long, R.T. Yang, J. Catal. 198 (2001) 20.
[40] R.Q. Long, R.T. Yang, J. Catal. 207 (2002) 224.
[41] B.R. Strohmeier, D.M. Hercules, J. Phys. Chem. 88 (1984) 4922.
[42] G. Qi, R.T. Yang, J. Phys. Chem. B 108 (2004) 15738.
[43] B. Liu, H. Nakatani, M. Terano, J. Mol. Catal. A 184 (2002) 387.
[44] J. Sainio, M. Eriksson, J. Lahtinen, Surf. Sci. 532–535 (2003) 396.
[45] A. Trunschke, D.L. Hoang, J. Radnik, H. Lieske, J. Catal. 191 (2000) 456.
[46] N. Russo, D. Fino, G. Saracco, V. Specchia, J. Catal. 229 (2005) 459.
[47] G. Karamullaoglu, T. Dogu, Ind. Eng. Chem. Res. 46 (2007) 7079.
[48] D.L. Hoang, S. Farage, A. Dittmar, A. Trunschke, H. Lieske, A. Martin, Catal. Lett. 112 (2006) 173.
[49] S. Ponce, M.A. Peña, J.L.G. Fierro, Appl. Catal. B 24 (2000) 193.
[50] F.C. Buciuman, F. Patcas, T. Hahn, Chem. Eng. Process. 38 (1999) 563.